

Electrically driven non-volatile resistance switching between charge density wave states at room temperature

R. Venturini^{1,2,*}, M. Rupnik^{3,4}, J. Gašperlin^{1,3}, J. Lipič^{1,3}, P. Šutar¹, Y. Vaskivskiy¹, F. Ščepanović^{1,3},
D. Grabnar¹, D. Golež^{1,3}, D. Mihailovic^{1,4}

¹Jozef Stefan Institute, 1000 Ljubljana, Slovenia

²PSI Center for Photon Science, Paul Scherrer Institute, 5232 Villigen PSI, Switzerland

³Faculty of Mathematics and Physics, University of Ljubljana, 1000 Ljubljana, Slovenia

⁴CENN Nanocenter, 1000 Ljubljana, Slovenia

* Correspondence to: rok.venturini@psi.ch

(Dated: December 17, 2024)

Control over the novel quantum states that emerge from non-equilibrium conditions is of both fundamental and technological importance. Metastable charge density wave (CDW) states are particularly interesting as their electrical manipulation could lead to ultra-efficient memory devices. However, the ability to use electrical pulses for non-volatile resistance switching involving CDW states is exceedingly rare and has been limited to cryogenic temperatures. In this work, we investigate a recently discovered layered semiconductor EuTe_4 that exhibits competition between distinct CDW orders that are susceptible to optical manipulation. We report that electrical pulses can be used for excitation to hidden, yet stable electronic states over a broad temperature range between 6 K and 400 K. We find that resistance switching is driven primarily by an electrical field and is fully reversible via a thermal erase procedure. Our experiments show that the pathway for switching is both fast and non-thermal. The resistance of the new electronic state is tuneable by the electrical pulse voltage, so the electronic device acts as a memristor. Our work opens the door for the non-thermal room temperature electrical control of the CDW order and holds great promise for novel memory devices and neuromorphic computing applications.

Introduction

The rapid growth of artificial neural networks has drastically increased computational demands but is hindered by their inefficiency when implemented on conventional von Neumann architectures. This has driven the development of beyond-CMOS technology that could implement fast, energy-efficient artificial neurons and synapses¹. A crucial component in neuromorphic computing is the memristor, which enables information storage and manipulation by controlling channel resistance.

Traditional memristor approaches rely on the transport of ions through solids, an inherently slow and often unreliable process². Promising emerging memristor technologies such as phase-change memory³ and Mott switches⁴⁻⁶ rely on transforming the atomic lattice via Joule heating across a structural phase

transition. This results in energy-inefficient and abrupt switching, deviating from the ideal linear resistance programming expected of artificial synapses^{3,7}. A novel approach is resistance switching between distinct charge density wave (CDW) states demonstrated in 1T-TaS₂^{8,9}. As such switching is based on changes to the electronic instead of structural order, memristive switching in 1T-TaS₂ was shown to be ultrafast¹⁰ and ultraefficient^{8,11,12} with high endurance¹¹. However, the non-volatile switching is limited to cryogenic temperatures¹³, which has motivated the exploration of CDW metastability in other materials.

Optical and electrical pulse excitation has become a promising route for accessing novel charge-ordered states that form in out-of-equilibrium conditions¹⁴⁻²¹. The lifetime of such states is generally limited to the picosecond timescale^{15,21-23}, as it is exceedingly rare to obtain a sufficiently high energy barrier between distinct CDW states for long-lived metastability. Pulse switching in 1T-TaS₂ has remained an exception to the rule, where stability on laboratory timescales and at cryogenic temperatures is provided via the pulse-induced topologically protected network of CDW domains and domain walls²⁴. Retaining novel charge-ordered states through metastability is not only interesting for potential applications, but it also offers a rare opportunity to study thermodynamically inaccessible quantum states.

In this work, we investigate EuTe₄, a recently discovered layered semiconductor with intricate CDW physics²⁵. The electronic states close to the Fermi surface originate from both single and bilayer square tellurium sheets (Fig. 1a and 1b) that provide a highly anisotropic Fermi surface susceptible to Fermi surface nesting²⁵⁻²⁸. The close-to-commensurate unidirectional CDW along the *b* axis (Fig. 1d) is observed at room temperature²⁸ with a transition temperature of 652 K²⁹. Recent works have uncovered additional in-plane CDW physics with CDW domains oriented along the *a* axis^{29,30} and domains with tilted CDW with respect to the atomic lattice³⁰. Further complexity is added to the system by the out-of-plane degree of freedom as the bilayer sheets are aligned, while the monolayer is staggered with respect to bilayers (Fig. 1a). While band calculations predict metallic behavior in the high-temperature state^{25,30}, the coexistence of multiple CDW orders is experimentally reflected in the anomalous transport of EuTe₄ showing semiconducting behavior with a giant hysteresis loop around room temperature. Competition and/or coexistence of distinct CDW orders makes EuTe₄ a promising candidate for exploring long-lived CDW metastabilities.

A breakthrough experiment demonstrated that ultrafast laser pulses can be used for non-volatile switching of the EuTe₄ resistance at room temperature³¹. While optical pulses of moderate fluence kept the resistance of the material within the hysteresis loop, high-fluence pulses could be used for switching outside the hysteresis loop. The ultrafast detection of a second harmonic signal has shown that following a laser pulse excitation, the CDW order evolves on an ultrafast timescale. Possible direct manipulation of the CDW states via the electrical pulses could open a new pathway to control CDW states at room temperature, and enable the fabrication of a fast and ultraefficient memristor.

Results

In this work, we report electrical pulse switching to novel CDW states that are exceptionally stable and therefore allow memristive operation of the EuTe_4 device at room temperature. The devices (schematically shown in Fig. 1c) are fabricated via a standard optical lithography (see Methods). Fig. 1d shows the resistance measurement of device D1 which exhibits an insulating and hysteretic behavior characteristic of EuTe_4 crystals. By using a current source to apply a 100 μA (2.7 V) current pulse to the cooling branch at 300 K, we observe a jump in resistance to a value that is well outside of the hysteresis loop. The new state is a thermodynamically inaccessible hidden state as it can't be reached via thermal cycling. As shown in Fig. 1e, the initial state is reversible by performing a thermal cycle up to 430 K.

Given the surprising stability of the novel state, we next explore its thermal stability at an even higher temperature of 350 K. In the inset of Fig. 1e, we show switching with a 2.0 V voltage pulse which is again applied to the cooling branch. Despite the high temperature, the novel state is remarkably stable during the next 15 hours (the duration of the experiment).

In Fig. 2 we present the details of the electrical switching behavior on device 2 (D2) at 300 K. Fig. 2a shows a systematic study of switching by increasing the electrical pulse voltage by starting either at the cooling or heating branch. We observe distinct behavior for low-voltage and high-voltage pulses, so we separate the response into two regimes. For the low-voltage regime, we observe that the resistance is continually increased by starting at the cooling branch, while the resistance decreases by starting from the heating branch. In the high-voltage regime, the resistance has a very similar value independent of the starting state and continually increases with increasing voltage. This indicates that in the low-voltage regime, the CDW has not yet fully transitioned to the novel state, partially retaining its history (original order), which is fully erased when switching in a high-voltage regime. Interestingly, the resistance of the EuTe_4 device gradually increases with increasing voltage which is in contrast to abrupt switching of CDW states observed in 1T-TaS_2 ⁸. To confirm that the value of resistance reached is a single shot effect and determined by the pulse amplitude, we apply a sequence of pulses with the same magnitude as shown in Supplementary Fig. 2. After a jump in resistance following the first pulse, there is no significant change to the state by adding further pulses of the same magnitude.

In Fig. 2b we present a current-voltage (IV) characteristic of the EuTe_4 device. To minimize Joule heating of the device, the current is applied in pulses while the voltage is measured during the current pulse. At low currents the device response is linear, while it starts to deviate above the linear extrapolation already at a low voltage of 0.2 V. This is consistent with the low-voltage onset of resistance switching shown in Fig. 2a. After reaching 1.0 V the current is gradually decreased with voltage following a linear response. Linear response is again observed by repeating the IV shot-by-shot measurement up to 1.0 V as shown in Supplemental Fig 3. This shows that the IV characteristic up to 1.0 V is linear and the deviation from linearity is due to resistance switching. The observed IV characteristic is completely different from an IV response of a semiconductor where significant Joule heating results in a sub-linear IV characteristic as shown in the inset to Fig. 2b. Absence of any sub-

linear behavior in the switching IV response demonstrates that switching is *non-thermal* and performed without significant heating of EuTe_4 .

To study the speed of switching, we apply voltage pulses of different lengths between 30 ns and 1 s and measure resistance before and after switching. As shown in Fig. 2c, we observe that switching is remarkably consistent over more than seven orders of magnitude. While thermal load increases significantly by increasing the pulse length, our experiments show that switching is completely independent of the pulse length, which is another confirmation of the non-thermal nature of switching. This also implies that switching is done by the leading edge of the pulse, the rise time of which is presently limited to 30 ns by our circuit (see Supplemental Fig. 5).

As we understand that switching can be triggered with very short pulses, we aim to explore how fast the system settles into the final state. To observe a change in resistance on short timescales we use short current pulses and observe the voltage over the device during the pulse with an oscilloscope. As shown in Fig. 2d, we observe that the high resistance state is already reached during the current pulse's rise time. We see this by comparing the observed voltage trace to the simulated response which assumes no resistance switching during the pulse (see Supplementary material for further details). The limitation of the current source rise time allows us to set the upper boundary for reaching the final state to the sub-microsecond timescale; however, the process is likely much faster.

Next, we explore the electrical switching behavior over a broad range of temperatures between 6 K and 300 K. As shown in Fig. 3a, we use low-voltage electrical pulses for which the change in resistance is moderate and at room temperature within the hysteresis loop. We might expect that the resistance change after applying an electrical pulse would be smaller at lower temperatures, where the hysteresis shrinks. However, as shown in Figs. 3b and 3d, the opposite happens: at low temperatures, driving even with low voltage is sufficient to switch the sample to hidden electronic states that lay outside of the hysteresis loop (see also Supplemental Fig. 7). Note that at low temperatures the voltage pulse drives significantly lower current due to a higher device resistance, which means any potential Joule heating effects are even further reduced.

In Fig. 3b we show temporal stability at different temperatures after applying the voltage pulse. We observe that the new state is remarkably stable on the laboratory timescale throughout the explored temperature range. Next, we perform pulsed IV measurements at both high temperatures and low temperatures (see Figs. 3c and 3d). Superficially, the response at all temperatures is similar: after a linear response at low currents, the response goes above the linear extrapolation, which signifies resistance switching. The IV characteristic obtained at 400 K deviates from this behavior at high currents, which we attribute to Joule heating. We observe that at low temperatures the magnitude of resistance switching is significantly higher and the switching itself behaves in a much more discrete way, with significant jumps on the IV plot.

The question of whether state switching in EuTe_4 is driven by an electric field or charge injection can be addressed by tracking switching parameters for different temperatures aided by the fact that the

resistance of the device significantly changes with temperature. To determine the switching voltage and current quantitatively, we fit the linear part of the IV curve and record threshold values where the IV curve deviates from linearity. As shown in Fig. 3e, the threshold current for switching is reduced significantly as the temperature is lowered, while the threshold voltage remains of a similar value throughout the explored temperature range. This strongly suggests that the electric field drives the electrical switching and not the current injection.

Discussion

Electrical manipulation of the CDW state in EuTe_4 appears highly efficient, as the observed switching voltage is surprisingly small, given the large device size. For the 30 ns pulses applied at room temperature, we calculate that the total energy deposited to the device is only 13 pJ, which limits the temperature increase during the pulse to 7 K (see SI for further details). We summarize some additional observations that support the non-thermal behavior of switching. (1) Switching is completely independent of the pulse length (see Fig. 2c) which is inconsistent with Joule-heating-driven switching^{3,32}. (2) The IV characteristic of a semiconductor affected by Joule heating would have a sub-linear response due to lower resistance at increased temperature³². We do not observe such a response in our measurements (see Fig 2d). (3) In a thermal scenario, the dissipated power during the switching should increase with a lowering temperature to provide sufficient heat for switching. In contrast, we see that at lower temperatures, the switching current is significantly lower compared to room temperature operation. (4) By performing a thermal heating cycle, the device resistance is monotonically reduced, regardless of the initial state (see Supplemental Fig 1). Switching with electrical pulses has the opposite effect of increasing the device resistance.

Our observations indicate that electrically driven CDW switching in EuTe_4 is very different from conventional switching experiments that drive the ordered equilibrium phase through a quench-like process to a high-temperature-like disordered state³. The response at room temperature is qualitatively similar to previous optical switching experiments, however, large fluences used for optical switching inescapably result in significant heating of the material³¹. The absence of abrupt switching and gradual change in resistance indicate that the free-energy landscape of CDW states is very complex, with many local minima that are separated by a high energy barrier.

We now turn to the microscopic origin of these local minima. Our strategy is to apply Peierls' theory of charge-density waves³³ to a microscopic model of EuTe_4 . We begin with a monolayer model and later include various interlayer stacking configurations to understand the energetics of excited states (see Methods). First, our calculation confirms that for the monolayer, the Lindhard response exhibits a peak very close to $\mathbf{q} = (1/3a, 1/3a)$, where a is the monolayer unit cell size, consistent with previous findings^{25,34}. For simplicity, we assume a commensurate wavevector and parameterize the distortion using the parameter α (see Fig. 1b), which is determined self-consistently (see Methods). In contrast to previous Density-functional theory calculations²⁵, the band structure of the monolayer CDW state is now completely gapped, and its energy landscape has minima at positive ($\alpha > 0$) and negative ($\alpha < 0$) distortions, which are symmetry-related and thus degenerate (see Fig. 4a).

Next, we examine the energetics of interlayer stacking. EuTe_4 exhibits two relevant stacking configurations: aligned bilayers and staggered monolayer Te sheets, see Fig. 1a. Since the bilayer and monolayer are separated by Eu-Te layers, their coupling acts as a weak link. We assume a fixed bilayer structure (green and orange layers in Fig. 4b and 4c) and vary the monolayer distortion α . There is a stable configuration for $\alpha < 0$ and a metastable configuration for $\alpha > 0$ (see Fig. 4a–c). These configurations are similar to states proposed for the lower and upper hysteresis within the Landau-Ginzburg description²⁸; however, our microscopic description enables an estimate of the potential barrier to several meV. This is consistent with experimental observations that weak excitations can switch the state, but the precise height of the barrier is challenging to estimate due to uncertainties in the microscopic parameters. Beyond this transition, we found other metastable minima at higher energies associated with various interlayer distortions (not shown). Additional experimental input is needed to determine which of these configurations are experimentally relevant.

Finally, we show that the interlayer stacking is coupled with the in-plane order by considering the Lindhard response of aligned or staggered bilayers' geometry, see Fig. 4(d)-(e). In both cases, the original peak close to $\mathbf{q}=(1/3a,1/3a)$ is split, showing maxima for collinear and noncollinear wave vectors³⁴. This means that the coupling between layers leads to a four-component charge-density wave forming nanostructures, as observed in previous STM experiments³⁰. This means that in-plane and out-of-plane orders are coupled and distortion of one would affect the other. Without further experiments, e.g. time-resolved diffractions^{35–37}, it is hard to conclude if the metastability originates from the interlayer stacking, destruction of the in-plane nanostructures, or coupling between the two.

Conclusion

In conclusion, we observe non-volatile resistance switching in EuTe_4 induced by electrical pulses over a broad temperature range. Remarkably, the switching is also possible outside of the thermal hysteresis loop, indicating that the electrical pulse-excited state is a thermally inaccessible hidden state. We find that switching requires only low voltage for operation despite the large size of our devices. This compares favorably with other emerging memristor technologies built on nm-sized devices that require several volts for operation^{3,38} and highlights the potential of further reducing the voltage for switching through nanoscale device fabrication, paving the way for ultra-efficient memristor applications. The nature of the hidden CDW states and their remarkable stability is still to be understood, offering a venue for a variety of further experiments. The experiments presented here open the question of a detailed mechanism for the non-thermal switching, which we hope will inspire investigations of the dynamics in the non-equilibrium regime.

Acknowledgments

We thank T. Mertelj, I. Vaskivskiy, V. Kabanov, and A. Mraz for fruitful discussions. We thank D. Vengust for his assistance with crystal characterization. D. M. wishes to acknowledge funding from ERC AdG ‘HIMMS’ and the Slovenian Research and Innovation Agency (ARIS) for programs N1-0290 and N1-0295. R. V., Y. V., and D. M. thank ARIS for funding the research program P1-0400. R.

V. acknowledges funding from the Swiss National Science Foundation (SNSF) and ARIS as a part of the WEAVE framework Grant Number 213148. D. Golež acknowledges the support of programs No. P1-0044, No. J1-2455 and MN-0016-106 of the ARIS.

Author Contributions

D. M. and D. Golež supervised the project. R. V. conceived the experiments. P. S. grew EuTe_4 crystals. R. V., M. R., and J. L. fabricated the devices. R. V., M. R., J. L., and D. Grabnar conducted electrical device measurements. J. G. and D. Golež performed theoretical calculations. R. V. and D. Golež wrote the paper with input from all co-authors.

Competing interests

The authors declare no competing interests.

Methods

EuTe₄ crystal growth. Single crystals of EuTe_4 were grown via a flux method. Europium pieces (99.99 %) and tellurium powder (99.999 %) were mixed in a ratio of 1:15 and put into a quartz ampule. The ampule was evacuated, sealed, and put into a cube furnace positioned nearly vertically. The furnace was heated over eight hours to reach 850 °C, then annealed for two days. After annealing, it was cooled over 100 hours to just above the melting point of the tellurium flux and held at this point for one week. The molten flux was then decanted, and the ampule was cooled. The resulting crystals are millimeter-sized and exhibit a golden, mirror-like surface. The crystal structure was confirmed by single-crystal X-ray diffraction.

Device fabrication. The circuits were fabricated via standard optical lithography using the photoresists LOR3A and S1805. Metallic electrodes were made using an e-beam evaporator by first depositing 3 nm of Ti, followed by 100 nm of Au. Liftoff was performed in mr-rem 700, followed by rinsing in isopropanol. Device D1 was made by exfoliating the EuTe_4 directly on the pre-fabricated circuit, which allowed us to avoid further chemical processing for that device. Device D2 was fabricated via the standard procedure of first exfoliating the EuTe_4 flake on Si/SiO₂ substrate followed by the lithography procedure described above. The entire device fabrication process (except for laser patterning) was done in an N₂-filled glovebox to avoid device degradation. All device experiments were done in high vacuum. Both devices D1 and D2 show similar switching behavior.

Device measurement and switching. The resistance measurements of devices were done via a standard 4-probe technique with Keithley 6221 current source and Keithley 2182A voltmeter. Pulsed electrical experiments were done either with current pulses from the Keithley 6221 or by voltage pulses from the Siglent SDG1050 function generator.

Theory

Tight-binding model. We describe the near-square Te layers in EuTe₄, which participate in the low-energy physics of interest¹⁸, using a minimal tight-binding model^{21,43}. We consider a square lattice, with two orthogonal p -type orbitals per site (p_x and p_y), nearest neighbour hopping and a filling of $2/3$. The in-plane electronic Hamiltonian is

$$H_{\parallel} = \sum_{\mathbf{k}} \varepsilon_x(\mathbf{k}) c_{\mathbf{k}}^{\dagger} c_{\mathbf{k}} + \varepsilon_y(\mathbf{k}) d_{\mathbf{k}}^{\dagger} d_{\mathbf{k}}$$

with electronic dispersions

$$\varepsilon_x(\mathbf{k}) = -2t_{\sigma} \cos(k_x a) - 2t_{\pi} \cos(k_y a)$$

$$\varepsilon_y(\mathbf{k}) = -2t_{\sigma} \cos(k_y a) - 2t_{\pi} \cos(k_x a)$$

where $c_{\mathbf{k}}^{\dagger}$ and $d_{\mathbf{k}}^{\dagger}$ are the creation operators for the p_x and p_y orbitals at momentum \mathbf{k} respectively. The parameters used are $t_{\sigma} = -2$ eV for end-on hopping, $t_{\pi} = 0.2$ eV for side-on hopping, and $a = 3.2341$ Å for the lattice constant of the square Te layers (note that this is not the same as the lattice constant of the full EuTe₄ structure, which is roughly $\tilde{a} \approx \sqrt{2}a$).

Interlayer hybridisation. We distinguish between an aligned bilayer configuration, where sites (m, n) of the two layers are shifted by $(0, 0, c)$, and a staggered bilayer configuration, where they are shifted by $(a/2, a/2, c)$. The interlayer coupling between neighbouring layers l and $l + 1$ enters the electronic Hamiltonian as

$$H_{\perp} = \sum_{\mathbf{k}} (t_{\perp}(\mathbf{k}) c_{\mathbf{k},l}^{\dagger} c_{\mathbf{k},l+1} + \text{h.c.}) + (t_{\perp}(\mathbf{k}) d_{\mathbf{k},l}^{\dagger} d_{\mathbf{k},l+1} + \text{h.c.})$$

$$t_{\perp}(\mathbf{k}) = \begin{cases} -t_{\text{al}} & \text{aligned geometry} \\ -t_{\text{st}}(1 + e^{ik_x a})(1 + e^{ik_y a})e^{-\frac{i}{2}(k_x + k_y)a} & \text{staggered geometry} \end{cases}$$

For the energy surface calculation in Fig. 4a, we use a rough estimate $t_{\text{al}} = 0.1$ eV and $t_{\text{st}} = 0.05$ eV, while for the Lindhard response shown in Fig. 4d,e, we use $t_{\text{al}} = 0.3$ eV and $t_{\text{st}} = 0.1$ eV.

Lindhard response. The optical susceptibility is computed on a discrete grid of N_k momentum points for each of the d dimensions using

$$\chi^R(\mathbf{q}, \omega) = \frac{1}{(N_k)^d} \sum_{\mathbf{k}} \sum_{m,n} \frac{f_m(\mathbf{k} + \mathbf{q}) - f_n(\mathbf{k})}{\omega + i\eta + \varepsilon_m(\mathbf{k} + \mathbf{q}) - \varepsilon_n(\mathbf{k})} \sum_{i\alpha} U_{im}(\mathbf{k} + \mathbf{q}) U_{\alpha m}^*(\mathbf{k} + \mathbf{q}) U_{\alpha n}(\mathbf{k}) U_{in}^*(\mathbf{k})$$

where m and n are band indices, $\varepsilon_m(\mathbf{k})$ is the corresponding band dispersion, $f_m(\mathbf{k}) = f(\varepsilon_m(\mathbf{k}))$ is the Fermi-Dirac distribution function and the matrix $\mathbf{U}(\mathbf{k})$ is a matrix of the column eigenvectors of the Hamiltonian matrix $\mathbf{h}(\mathbf{k})$. The broadening parameter is set to $\eta = 10^{-8}$ and we investigate the static response, i.e., $\omega = 0$.

Lattice distortion and Peierls coupling. The displacement of site (m, n) is parametrised as a periodic lattice distortion (PLD) of the form

$$u_{m,n} = \frac{2\alpha a}{\sqrt{3}} \begin{pmatrix} \sin(\mathbf{q} \cdot \mathbf{R}_{m,n} + \theta_x) \\ \sin(\mathbf{q} \cdot \mathbf{R}_{m,n} + \theta_y) \end{pmatrix}$$

with the CDW wave vector \mathbf{q} , equilibrium lattice positions $\mathbf{R}_{m,n} = a(m, n)$ [for staggered geometry $\mathbf{R}_{m,n} = a(m, n) + \frac{a}{2}(1,1)$], the amplitude α (given as a fraction of the lattice constant) and two phase parameters, θ_x and θ_y . The electronic and lattice degrees of freedom are coupled via Peierls coupling, where the in-plane hopping is linearly suppressed with α . This extends the electronic Hamiltonian with the following terms

$$H_{\text{el-lat}} = \sum_{m,n} [t_\sigma g_\sigma x_{m,n} (c_{m,n}^\dagger c_{m+1,n} + \text{h.c.}) + t_\pi g_\pi y_{m,n} (c_{m,n}^\dagger c_{m,n+1} + \text{h.c.}) \\ + t_\sigma g_\sigma y_{m,n} (d_{m,n}^\dagger d_{m,n+1} + \text{h.c.}) + t_\pi g_\pi x_{m,n} (d_{m,n}^\dagger d_{m+1,n} + \text{h.c.})]$$

where $x_{m,n} = \|\mathbf{r}_{m+1,n} - \mathbf{r}_{m,n}\|$ (similar for $y_{m,n}$; here $\mathbf{r}_{m,n} = \mathbf{R}_{m,n} + \mathbf{u}_{m,n}$) and the coupling parameter is estimated, by a qualitative fit to the experimental lattice distortion, as $g_\sigma = g_\pi = 0.53 \text{ \AA}^{-1}$. We assume softening of a single phonon mode corresponding to a PLD commensurate with the square lattice, i.e., $q = \frac{a^*}{3}(1,1)$. Moving to k -space and utilising the PLD parametrisation as a mean-field approximation, we obtain the effective electronic Hamiltonian for a single layer

$$H_{\text{el}} = \sum_{\mathbf{k}} \mathbf{c}_{\mathbf{k}}^\dagger \mathbf{h}_x(\mathbf{k}) \mathbf{c}_{\mathbf{k}} + \mathbf{d}_{\mathbf{k}}^\dagger \mathbf{h}_y(\mathbf{k}) \mathbf{d}_{\mathbf{k}}$$

where

$$\mathbf{h}_x(\mathbf{k}) = \begin{pmatrix} \varepsilon_x(\mathbf{k}) & \Delta_x^*(\mathbf{k}) & \Delta_x(\mathbf{k} + 2\mathbf{q}) \\ \Delta_x(\mathbf{k}) & \varepsilon_x(\mathbf{k} + \mathbf{q}) & \Delta_x^*(\mathbf{k} + \mathbf{q}) \\ \Delta_x^*(\mathbf{k} + 2\mathbf{q}) & \Delta_x(\mathbf{k} + \mathbf{q}) & \varepsilon_x(\mathbf{k} + 2\mathbf{q}) \end{pmatrix} \quad \mathbf{c}_{\mathbf{k}} = \begin{pmatrix} c_{\mathbf{k}} \\ c_{\mathbf{k}+\mathbf{q}} \\ c_{\mathbf{k}+2\mathbf{q}} \end{pmatrix}$$

and the CDW order parameter is

$$\Delta_x(\mathbf{k}) = -2ia\alpha \left[t_\sigma g_\sigma \cos\left(k_x a + \frac{qa}{2}\right) e^{i(\theta_x - \pi/2)} + t_\pi g_\pi \cos\left(k_y a + \frac{qa}{2}\right) e^{i(\theta_y - \pi/2)} \right]$$

and similar for $\mathbf{h}_y(\mathbf{k})$, \mathbf{d}_k and $\mathbf{\Delta}_y(\mathbf{k})$. The lattice energy per site is computed using the harmonic approximation as $H_{\text{lat}} = 2Ka^2\alpha^2$, with the lattice constant estimated²⁸ as $K = 1.44 \text{ eV/\AA}^2$. The dimensionless parameter quantifying the strength of the electron-lattice response is thus $t_\sigma g/Ka \approx 0.23$.

Numerical simulations. The numerical simulations were implemented in Python with aid of the NumPy and SciPy modules. A k -point grid of 200×200 points was determined to be sufficiently accurate for the energy surface calculations, while a 300×300 grid was used for computing the Lindhard response. The optimization w. r. t., $(\alpha, \theta_x, \theta_y)$ was performed by using the modified Powell method to obtain the roots of the equilibrium condition equation, which in turn was derived using the Hellmann-Feynman theorem. The accuracy threshold for the PLD parameters was set to $\epsilon = 10^{-5}$. It is important to emphasize that the degeneracy for monolayer, Fig.4a, arises only when each configuration is relaxed with respect to the phase of the charge-density wave in both the x and y directions at a given distortion α .

References

1. Mehonic, A. & Kenyon, A. J. Brain-inspired computing needs a master plan. *Nature* **604**, 255–260 (2022).
2. Sun, W. *et al.* Understanding memristive switching via in situ characterization and device modeling. *Nat Commun* **10**, 3453 (2019).
3. Park, S.-O. *et al.* Phase-change memory via a phase-changeable self-confined nano-filament. *Nature* **628**, 293–298 (2024).
4. Hoffmann, A. *et al.* Quantum materials for energy-efficient neuromorphic computing: Opportunities and challenges. *APL Materials* **10**, 070904 (2022).
5. Janod, E. *et al.* Resistive Switching in Mott Insulators and Correlated Systems. *Adv Funct Materials* **25**, 6287–6305 (2015).
6. Cheng, S. *et al.* *Operando* characterization of conductive filaments during resistive switching in Mott VO₂. *Proc. Natl. Acad. Sci. U.S.A.* **118**, e2013676118 (2021).
7. Kim, S. J. *et al.* Linearly programmable two-dimensional halide perovskite memristor arrays for neuromorphic computing. *Nat. Nanotechnol.* (2024) doi:10.1038/s41565-024-01790-3.
8. Vaskivskiy, I. *et al.* Fast electronic resistance switching involving hidden charge density wave states. *Nat. Commun.* **7**, 11442 (2016).
9. Yoshida, M., Suzuki, R., Zhang, Y., Nakano, M. & Iwasa, Y. Memristive phase switching in two-dimensional 1T-TaS₂ crystals. *Sci. Adv.* **1**, e1500606 (2015).
10. Venturini, R. *et al.* Ultraefficient resistance switching between charge ordered phases in 1T-TaS₂ with a single picosecond electrical pulse. *Appl. Phys. Lett.* **120**, 253510 (2022).
11. Mraz, A. *et al.* Charge Configuration Memory Devices: Energy Efficiency and Switching Speed. *Nano Lett.* **22**, 4814–4821 (2022).
12. Mihailovic, D. *et al.* Ultrafast non-thermal and thermal switching in charge configuration memory devices based on 1T-TaS₂. *Appl. Phys. Lett.* **119**, 013106 (2021).
13. Vaskivskiy, I. *et al.* Controlling the metal-to-insulator relaxation of the metastable hidden quantum state in 1T-TaS₂. *Sci. Adv.* **1**, e1500168–e1500168 (2015).

14. de la Torre, A. *et al.* *Colloquium: Nonthermal pathways to ultrafast control in quantum materials.* *Rev. Mod. Phys.* **93**, 041002 (2021).
15. Kogar, A. *et al.* Light-induced charge density wave in LaTe_3 . *Nat. Commun.* **16**, 159–163 (2020).
16. Domröse, T. *et al.* Light-induced hexatic state in a layered quantum material. *Nat. Mater.* **22**, 1345–1351 (2023).
17. Stojchevska, L. *et al.* Ultrafast Switching to a Stable Hidden Quantum State in an Electronic Crystal. *Science* **344**, 177–180 (2014).
18. Han, T.-R. T. *et al.* Exploration of metastability and hidden phases in correlated electron crystals visualized by femtosecond optical doping and electron crystallography. *Sci. Adv.* **1**, e1400173 (2015).
19. Gerasimenko, Y. A. *et al.* Quantum jamming transition to a correlated electron glass in 1T-TaS_2 . *Nat. Mater.* **18**, 1078–1083 (2019).
20. Murakami, Y., Golež, D., Eckstein, M. & Werner, P. Photo-induced nonequilibrium states in Mott insulators. Preprint at <https://doi.org/10.48550/ARXIV.2310.05201> (2023).
21. Duan, S. *et al.* Ultrafast Switching from the Charge Density Wave Phase to a Metastable Metallic State in $1\text{T}-\text{TiSe}_2$. *Phys. Rev. Lett.* **130**, 226501 (2023).
22. Zong, A. *et al.* Evidence for topological defects in a photoinduced phase transition. *Nature Physics* **15**, 27–31 (2019).
23. Maklar, J. *et al.* Nonequilibrium charge-density-wave order beyond the thermal limit. *Nat Commun* **12**, 2499 (2021).
24. Gerasimenko, Y. A., Karpov, P., Vaskivskyi, I., Brazovskii, S. & Mihailovic, D. Intertwined chiral charge orders and topological stabilization of the light-induced state of a prototypical transition metal dichalcogenide. *npj Quantum Mater.* **4**, 1–9 (2019).
25. Wu, D. *et al.* Layered semiconductor EuTe_4 with charge density wave order in square tellurium sheets. *Phys. Rev. Materials* **3**, 024002 (2019).
26. Zhang, Q. Q. *et al.* Thermal hysteretic behavior and negative magnetoresistance in the charge density wave material EuTe_4 . *Phys. Rev. B* **107**, 115141 (2023).

27. Zhang, C. *et al.* Angle-resolved photoemission spectroscopy study of charge density wave order in the layered semiconductor EuTe_4 . *Phys. Rev. B* **106**, L201108 (2022).
28. Lv, B. Q. *et al.* Unconventional Hysteretic Transition in a Charge Density Wave. *Phys. Rev. Lett.* **128**, 036401 (2022).
29. Rathore, R. *et al.* Evolution of static charge density wave order, amplitude mode dynamics, and suppression of Kohn anomalies at the hysteretic transition in EuTe_4 . *Phys. Rev. B* **107**, 024101 (2023).
30. Xiao, K. *et al.* Hidden Charge Order and Multiple Electronic Instabilities in EuTe_4 . *Nano Lett.* **24**, 7681–7687 (2024).
31. Liu, Q. *et al.* Room-temperature non-volatile optical manipulation of polar order in a charge density wave. *Nat Commun* **15**, 8937 (2024).
32. Chen, H., Wang, N., Liu, H., Wang, H. & Ravichandran, J. Charge-Density-Wave Resistive Switching and Voltage Oscillations in Ternary Chalcogenide BaTiS_3 . *Adv Elect Materials* **9**, 2300461 (2023).
33. Grüner, G. *Density Waves in Solids*. (CRC Press, Boca Raton London New York, 2019). doi:10.1201/9780429501012.
34. Pathak, A., Gupta, M. K., Mittal, R. & Bansal, D. Orbital- and atom-dependent linear dispersion across the Fermi level induces charge density wave instability in EuTe_4 . *Phys. Rev. B* **105**, 035120 (2022).
35. Laulhé, C. *et al.* Ultrafast Formation of a Charge Density Wave State in 1T-TaS_2 : Observation at Nanometer Scales Using Time-Resolved X-Ray Diffraction. *Physical Review Letters* **118**, (2017).
36. Vogelgesang, S. *et al.* Phase ordering of charge density waves traced by ultrafast low-energy electron diffraction. *Nat. Phys.* **14**, 184–190 (2018).
37. Verma, A. *et al.* Picosecond volume expansion drives a later-time insulator–metal transition in a nano-textured Mott insulator. *Nat. Phys.* **20**, 807–814 (2024).
38. Li, M. *et al.* Imperfection-enabled memristive switching in van der Waals materials. *Nat Electron* **6**, 491–505 (2023).

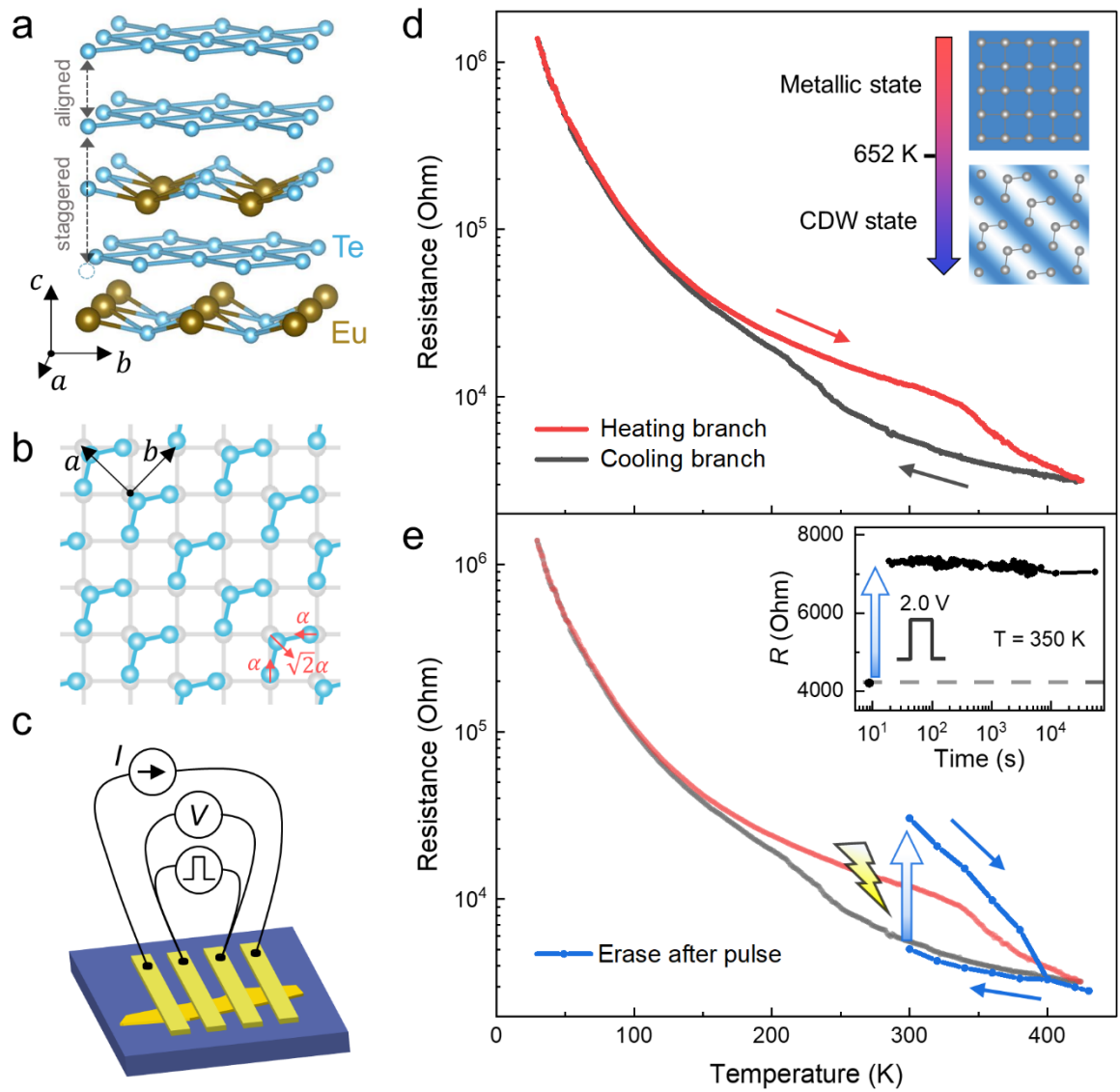


Fig. 1: EuTe₄ and electrical pulse switching on device D1. a) Crystal structure of EuTe₄. b) A square lattice of Te atoms is shown in gray, while a distorted lattice hosting CDW state is shown in blue. c) Illustration of a EuTe₄ electrical device with a current source, voltmeter, and voltage pulse source connected to the device. d) Thermal hysteresis of the EuTe₄ device during the cooling (black) and heating (red) process. The inset shows an illustration of the material phase diagram with the charge density modulation indicated by white stripes. e) Electrical switching with 2.7 V pulse and a subsequent state erase by heating to 430 K and cooling to room temperature (blue). The inset shows switching with a 2.0 V pulse at 350 K and the state stability.

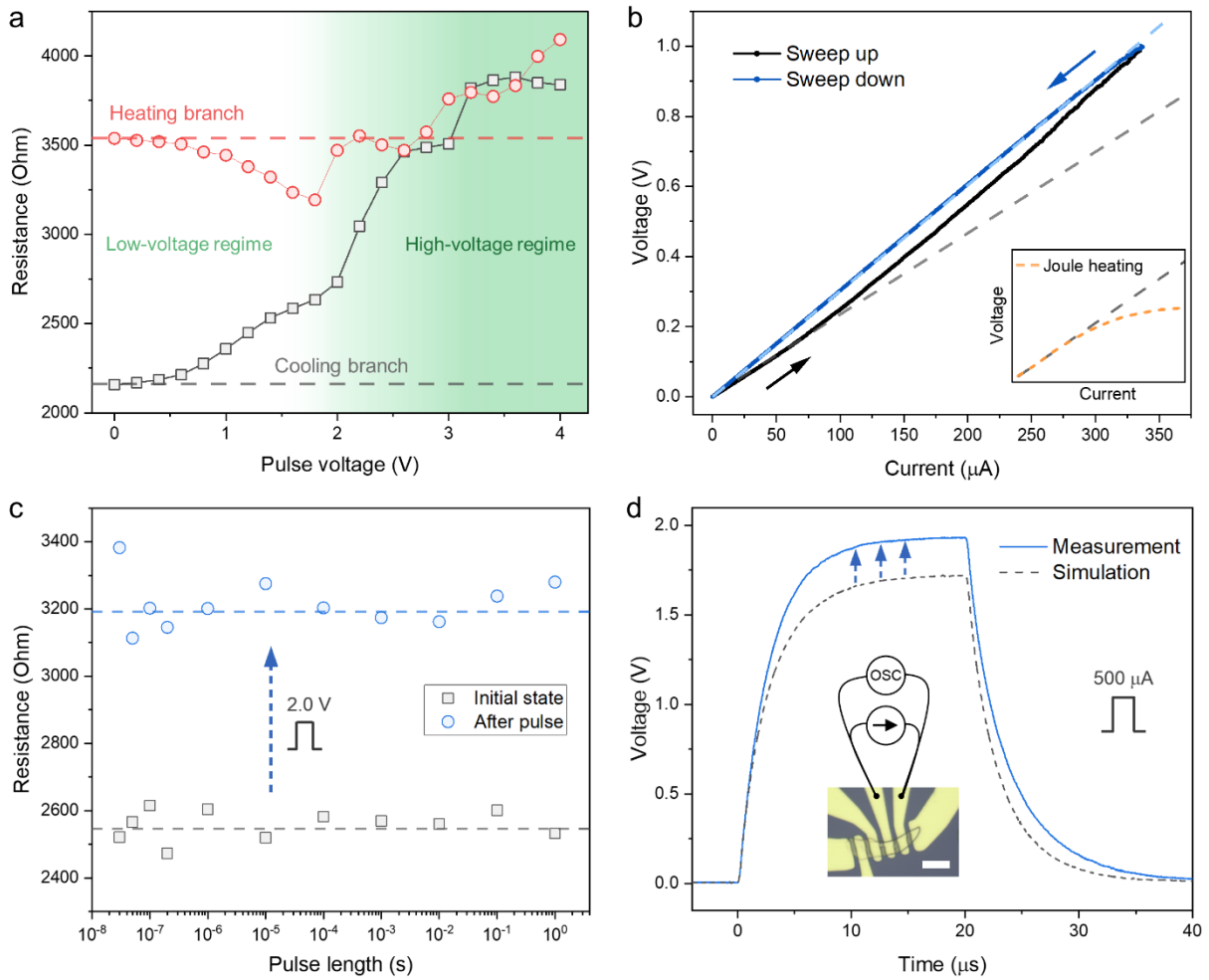


Fig. 2: EuTe₄ electrical switching of device D2 at 300 K . a) Device resistance after electrical pulses are applied to either the cooling branch (black) or the heating branch (red). We see a distinct response for low-voltage and high-voltage regimes. b), c), and d) Electrical pulse switching from the cooling branch. b) Voltage measured during the current pulses by incrementally increasing (black) and decreasing (blue) pulse magnitude. The dashed line is a linear fit to the low current region. The inset shows a sketch of a typical sub-linear IV response of a semiconductor due to Joule heating. c) Resistance switching by applying 2.0 V voltage pulses for different pulse lengths. d) Direct temporal observation of the switching process during a 500 μA current pulse. Measurement is compared to the simulated response that assumes no resistance change during the current pulse. Insert image shows a microscope image of the device with a current source and oscilloscope connections (scalebar: 10 μm).

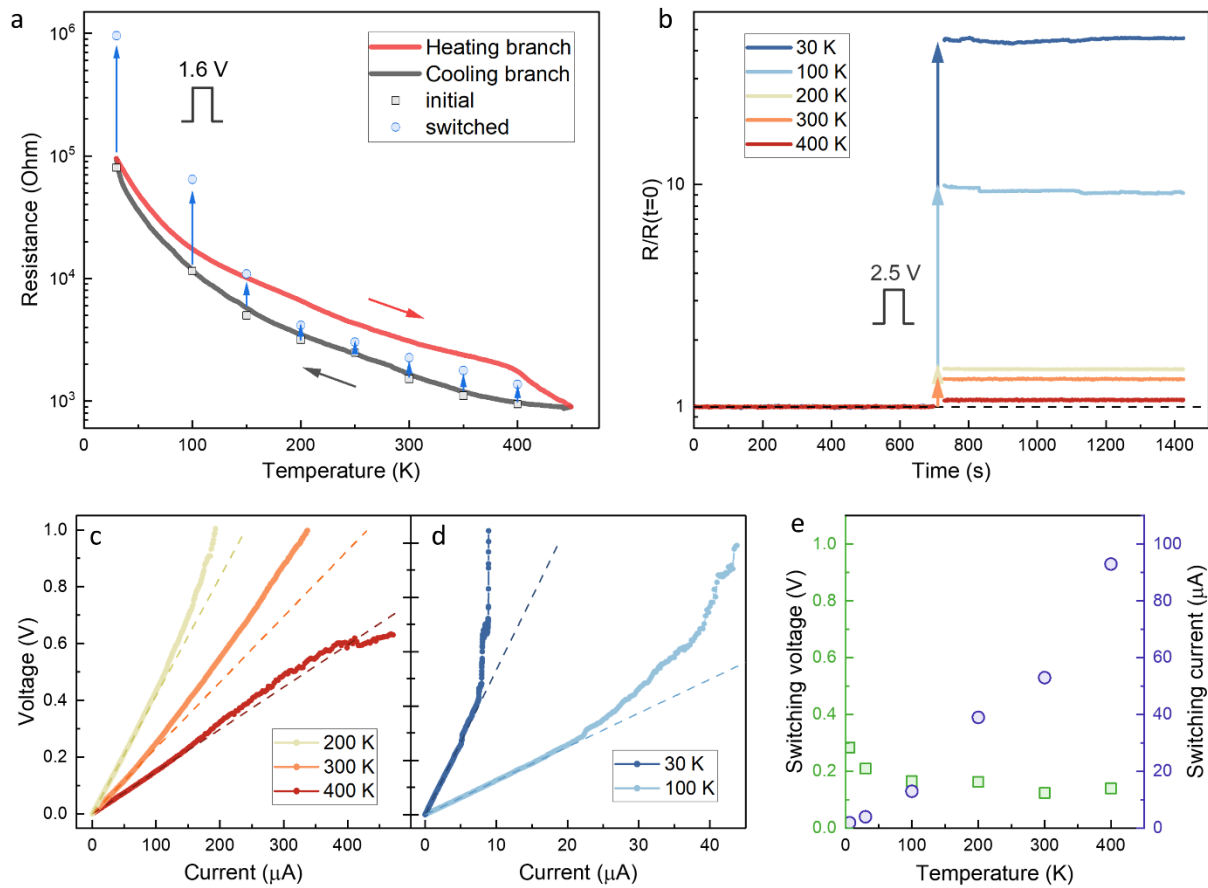


Fig. 3: Switching of device D2 from the cooling branch at different temperatures. a) Electrical switching with a low magnitude voltage pulse of 1.6 V at different temperatures. b) Stability of the state before and after switching. c) and d) Voltage measured during the current pulses by incrementally increasing pulse magnitude for high- and low-temperature regimes, respectively. e) Temperature dependence of the threshold voltage and current for switching.

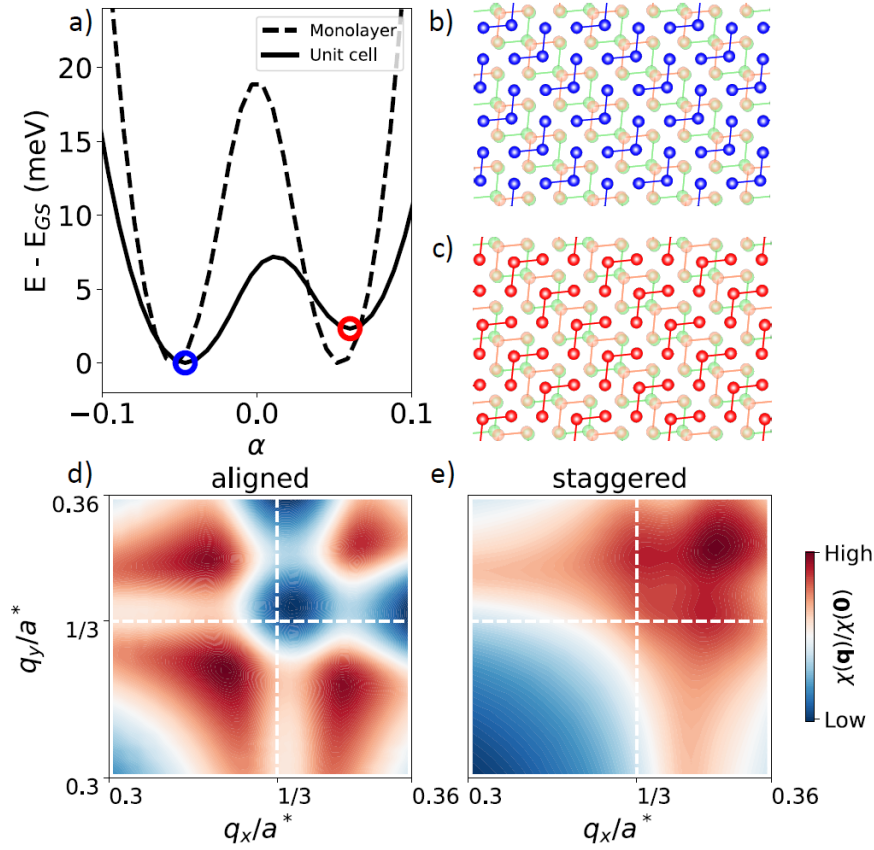


Fig. 4: Microscopic modeling of intralayer and interlayer patterns. a) The energy landscape versus the lattice distortion α of a monolayer system (dashed line) or the unit cell composed of three layers with fixed bilayer (full line). The blue and red circles mark the ground and metastable state, respectively. Corresponding real-space configurators are presented in b) and c), where the top (bottom) layer of the bilayer is shown in transparent orange (green). The Lindhard response for an undistorted aligned and staggered bilayer geometry is shown in d) and e).